Dalton Transactions

ROYAL SOCIETY OF CHEMISTRY

COMMUNICATION

View Article Online
View Journal | View Issue

Cite this: *Dalton Trans.*, 2024, **53**, 3470

Received 7th January 2024,
Accepted 31st January 2024

DOI: 10.1039/d4dt00043a

rsc.li/dalton

Electrocatalytic reduction of nitrite to ammonia on undercoordinated Cu†

Ruichao Zhang,* Shiyao Shang, Fuzhou Wang and Ke Chu *

Electrocatalytic NO_2^--to-NH_3 reduction (NO_2RR) has emerged as an intriguing route for simultaneous mitigation of harmful nitrites and production of valuable NH_3. Herein, we design for the first time undercoordinated Cu nanowires (u-Cu) as an efficient and selective NO_2RR electrocatalyst, delivering the maximum NO_2^--to-NH_3 faradaic efficiency of 94.7% and an ammonia production rate of 494.5 μmol h^{-1} cm^{-2} at −0.7 V *vs.* RHE. Theoretical calculations reveal that the created undercoordinated Cu sites on u-Cu can enhance NO_2^- adsorption, boost NO_2^--to-NH_3 energetics and restrict competitive hydrogen evolution, thereby enabling the active and selective NO_2RR.

Ammonia is an important feedstock for agricultural and industrial products.[1] To date, the main method for industrial NH_3 production is the traditional Haber–Bosch process, which consumes enormous amounts of energy and emits huge amounts of CO_2.[2] Electrochemical nitrogen fixation to ammonia (NRR) represents a clean and sustainable method for NH_3 synthesis.[3] Nevertheless, the extremely low N_2 solubility and very strong N≡N bond generally result in a very low NH_3 yield rate and N_2-to-NH_3 faradaic efficiency.[2–10]

Nitrite (NO_2^-) is known as a category A carcinogen and the excessive intake of NO_2^- can cause brain damage, cancer and other diseases, and thus the World Health Organization stipulates that the NO_2^- content in drinking water should be less than 3 ppm.[11] However, due to the extensive discharge of industrial wastewater and the use of nitrogen-containing fertilizers, a large amount of NO_2^- pollution is released to the environment, which not only seriously affects human health, but also disrupts the natural nitrogen cycle.[12–15] Encouragingly, considering that NO_2^- possesses much higher aqueous solubility and a weaker N=O bond than N_2, electrocatalytic NO_2^--to-NH_3 reduction (NO_2RR) has emerged as a promising route to simultaneously achieve hazardous NO_2^- removal and green NH_3 synthesis.[16–18] Nonetheless, efficient NO_2RR is still restricted by the competitive HER and complex six-electron process, and thus there is a strong need for the exploration of active and selective electrocatalysts to promote NO_2^--to-NH_3 reaction energetics and impede the HER.[19–29]

Recently, extensive studies have been conducted to develop a wide range of potential NO_2RR catalysts, including precious metals, non-precious metal compounds and single-atom catalysts.[30] Among them, Cu-based materials receive the most attention owing to their fascinating advantages of favorable NO_2^- activation, low cost and good stability.[31–33] Despite the significant advances, the NO_2RR performance of most reported Cu catalysts still falls behind people's expectations. Defect engineering of metal catalysts is considered as a facile but powerful strategy,[34–36] as it can create plentiful undercoordinated metal sites to significantly boost the adsorption and activation of reactive species and intermediates, resulting in enhanced electrocatalytic activity. Therefore, it is interesting to use a defect engineering strategy to design undercoordinated Cu catalysts with enhanced NO_2^--to-NH_3 efficiency.

Herein, undercoordinated Cu nanowires (u-Cu) are firstly demonstrated as a high-efficiency NO_2RR catalyst, delivering the maximum NO_2^--to-NH_3 faradaic efficiency (FE_{NH_3}) of 94.7% and an NH_3 yield rate of 494.5 μmol h^{-1} cm^{-2} at −0.7 V *vs.* RHE. The NO_2RR mechanism of u-Cu is further revealed by molecular dynamics (MD) simulations and density functional theory (DFT) calculations.

Pristine Cu was synthesized by thermal annealing reduction of CuO nanowires (grown on Cu foam) under an H_2/Ar atmosphere.[37] Plasma treatment was then conducted to construct undercoordinated Cu sites on pristine Cu to obtain u-Cu. The scanning electron microscopy (SEM, Fig. 1a and Fig. S1†) and transmission electron microscopy (TEM, Fig. 1b) images show that both Cu and u-Cu present quite similar features of nanowire morphology. The high-resolution transmission electron microscopy (HRTEM, Fig. 1c) image of u-Cu reveals a lattice interplanar distance of 0.205 nm, indicating the exposure of

School of Materials Science and Engineering, Lanzhou Jiaotong University, Lanzhou 730070, China. E-mail: zhangrch11@163.com, chuk630@mail.lzjtu.cn

† Electronic supplementary information (ESI) available. See DOI: https://doi.org/10.1039/d4dt00043a

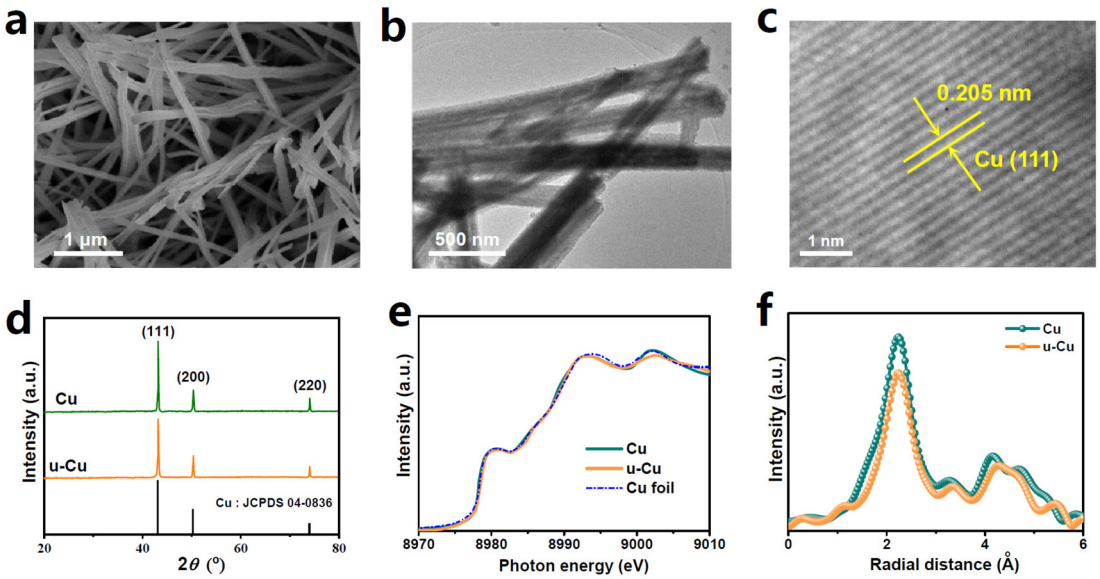

Fig. 1 (a) SEM image of u-Cu. (b) TEM image of u-Cu. (c) HRTEM image of u-Cu. (d) XRD patterns of Cu and u-Cu. (e) XANES spectra of Cu, u-Cu and the Cu foil reference. (f) EXAFS spectra of Cu and u-Cu.

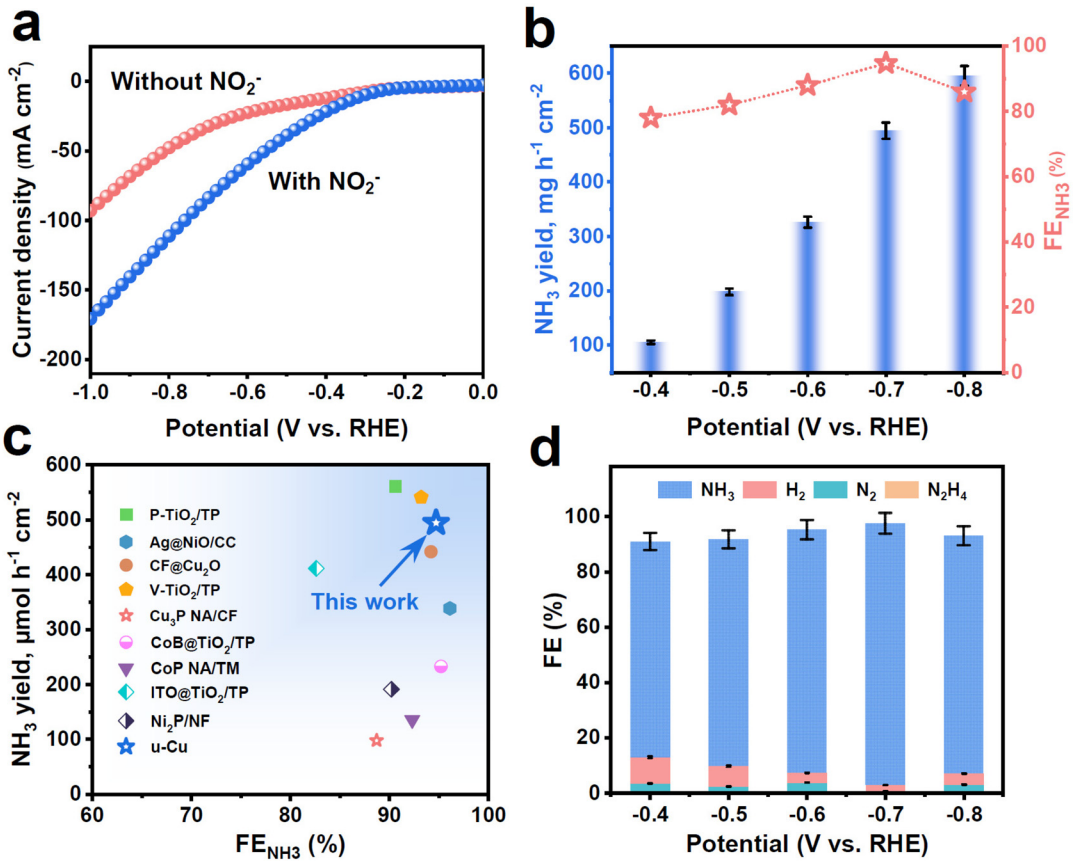

Fig. 2 (a) LSV curves of u-Cu under different conditions in a 0.5 M Na_2SO_4 + 0.1 M $NaNO_2$ electrolyte at a scan rate of 10 mV s^{-1}. (b) NH_3 yield rates and FE_{NH_3} of u-Cu at different potentials. (c) Comparison of the optimal NO_2RR performance between u-Cu and the reported catalysts. (d) FEs of various products at different potentials.

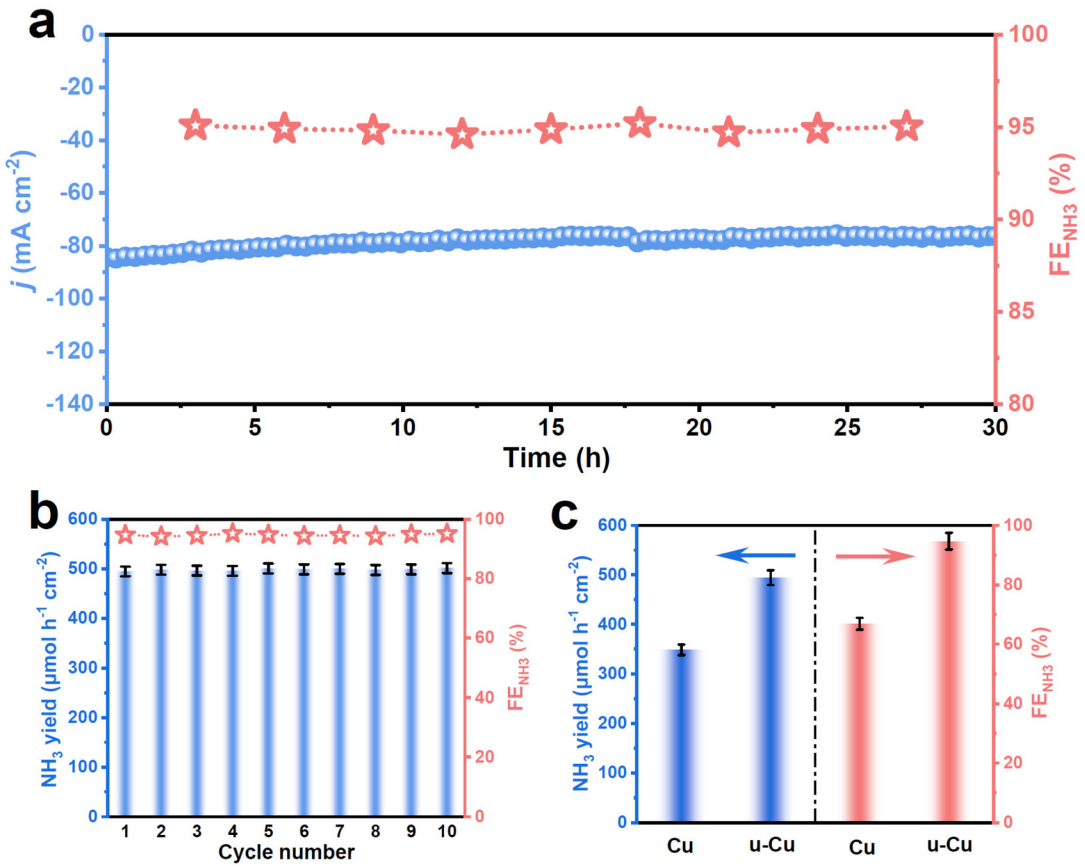

Fig. 3 (a) Chronoamperometry test of u-Cu at −0.7 V *vs.* RHE for 30 h of continuous electrolysis in a 0.5 M Na_2SO_4 + 0.1 M $NaNO_2$ electrolyte. (b) Cycling test of u-Cu at −0.7 V *vs.* RHE. (c) Comparison of the NO_2RR performance between Cu and u-Cu at −0.7 V *vs.* RHE.

the Cu (111) crystal facet. As shown in the X-ray diffraction (XRD, Fig. 1d) patterns, both Cu and u-Cu exhibit metallic Cu (Cu(0)) peaks of (111), (200) and (220) with the absence of Cu-oxide species (Cu(I)/Cu(II)), in line with the X-ray photoelectron spectroscopy (XPS, Fig. S2†) results. Likewise, the X-ray absorption near-edge spectroscopy (XANES, Fig. 1e) spectra show that both Cu and u-Cu exhibit nearly the same profiles as those of the Cu foil, indicating the metallic state of Cu and u-Cu. However, an obvious distinction can be found in the extended X-ray absorption fine structure (EXAFS, Fig. 1f) spectra, where u-Cu shows a much reduced Cu–Cu bond intensity compared to Cu,[38] suggesting that u-Cu is rich in undercoordinated Cu sites.

The electrocatalytic NO_2RR properties of u-Cu are examined in a 0.5 M Na_2SO_4 electrolyte with 0.1 M $NaNO_2$ using an H-shaped cell.[33] All potentials are converted into reversible hydrogen electrodes (RHE). Fig. 2a shows the linear sweep voltammetry (LSV) curves of u-Cu under different conditions in a 0.5 M Na_2SO_4 + 0.1 M $NaNO_2$ electrolyte at a scan rate of 10 mV s^{-1}, showing that u-Cu presents a much higher current density in a NO_2^--containing solution compared to a NO_2^--free solution, implying that u-Cu is highly active towards the NO_2RR. The NO_2RR performance of u-Cu is quantitatively assessed with the integration of chronoamperometric (Fig. S3†) and spectrophotometric methods (Fig. S4†). As displayed in Fig. 2b, the FE_{NH_3} of u-Cu increases with an increase in the negative potential, until it reaches a maximum value of 94.7% at the optimum potential at −0.7 V *vs.* RHE, where the corresponding NH_3 yield rate is 494.5 μmol h^{-1} mg^{-1}. As shown in Fig. 2c and Table S1,† the NO_2RR performance of u-Cu is higher than that of most previous NO_2RR electrocatalysts in terms of both FE_{NH_3} and NH_3 yield rate. Nonetheless, when the potential is increased to −0.8 V *vs.* RHE, the FE_{NH_3} is decreased sharply, primarily attributed to the increased HER at elevated potentials. Furthermore, as shown in Fig. 2d, FEs of by-products (H_2, N_2 and N_2H_4) are much lower than FE_{NH_3} at all considered potentials, suggesting an exceptional NO_2^--to-NH_3 selectivity of u-Cu.

Fig. S5† shows that the produced NH_3 can barely be detected at the open circuit potential (OCP) and in a NO_2^--free electrolyte, verifying that the generation of NH_3 only occurs *via* the u-Cu-catalyzed NO_2RR process. As for the stability of u-Cu during the electrochemical NO_2RR process, the continuous 20 h electrolysis showed negligible degeneration in FE_{NH_3} and the current density, confirming the good long-term stability of u-Cu (Fig. 3a). Besides, no distinct fluctuations in FE_{NH_3} and NH_3 yield rates were observable during ten consecutive cycles of electrolysis (Fig. 3b), attesting to a favorable cycling stability

of u-Cu. Obviously, the performance comparison (Fig. 3c) shows that u-Cu greatly outperforms Cu in both NH_3 yield rate and FE_{NH_3}, suggesting that plasma treatment to create under-coordinated Cu sites is critical in dramatically boosting the NO_2RR activity of Cu. By normalizing the NO_2RR performance with the electrochemically active surface area (ECSA, Fig. S6†),[14] the ECSA-normalized FE_{NH_3} and NH_3 yield rate of u-Cu are still significantly higher than those of Cu (Fig. S7†), manifesting the higher intrinsic NO_2RR activity of u-Cu than Cu.

The enhanced NO_2RR activity of u-Cu was then mechanistically investigated by theoretical computations. First, we evaluate NO_2^- adsorption on both Cu and u-Cu in the simulated electrolyte systems (Fig. S8†), as NO_2^- adsorption is a critical step to trigger the NO_2RR.[14,39,40] After the MD simulations, it is shown in Fig. 4a that the degree of NO_2^- accumulation on u-Cu is more obvious than that on Cu. Meanwhile, as revealed by the radial distribution function (RDF, Fig. 4b), the interaction between NO_2^- and u-Cu is notably stronger than that between NO_2^- and Cu.[41] These results demonstrate that NO_2^- adsorption and coverage are considerably enhanced in u-Cu, which is favorable for the following NO_2RR process.

We then analyzed the free energy diagram of the whole NO_2RR pathway. Fig. S9 and S10† show the corresponding atomic structures of various reaction intermediates on Cu and u-Cu. As depicted in Fig. 4c, pristine Cu shows two uphill steps

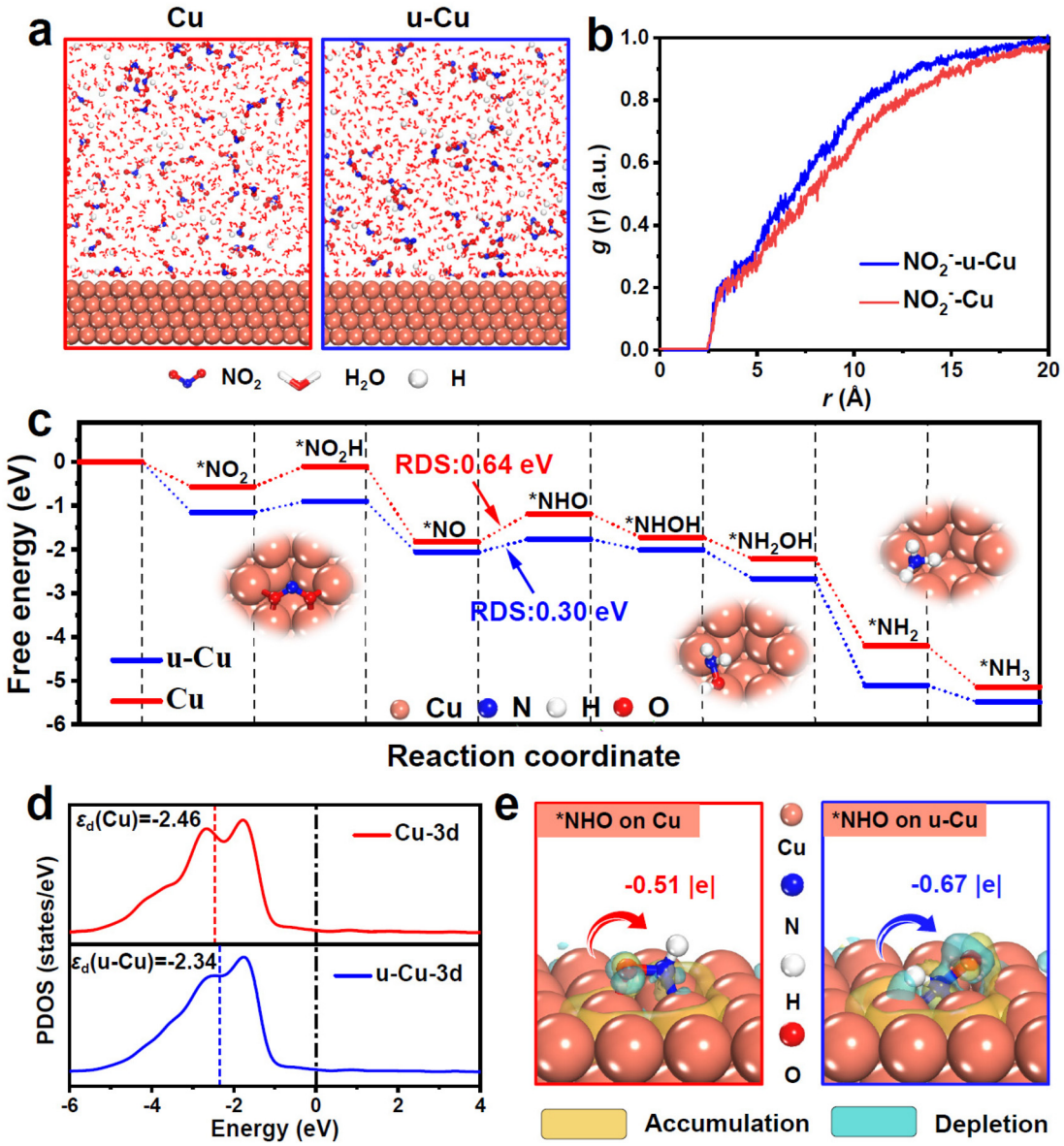

Fig. 4 (a) Snapshots of the dynamic adsorption process of $*NO_2$ on Cu and u-Cu after MD simulations, and the corresponding (b) RDF curves of the interactions between $*NO_2$ and Cu/u-Cu. (c) Free energy diagrams of the NO_2RR pathways on Cu and u-Cu. (d) PDOS profiles of Cu and u-Cu for calculating their d-band centers. (e) EDD maps of *NHO on Cu and u-Cu.

of $*NO_2 \rightarrow *NO_2H$ and $*NO \rightarrow *NHO$, where the latter serves as the rate-determining step (RDS) with the highest energy barrier of 0.64 eV. Promisingly, owing to the enhanced NO_2^- adsorption and coverage (Fig. 4a and b), $*NO_2 \rightarrow *NO_2H$ on u-Cu becomes downhill, while the RDS energy barrier of $*NO \rightarrow *NHO$ on u-Cu is reduced to 0.30 eV, suggesting that the NO_2RR energetics is greatly enhanced on u-Cu to favor NO_2^--to-NH_3 conversion. To reveal the underlying reasons, the integration of electron density difference (EDD) and partial density of states (PDOS) was carried out. The PDOS analysis (Fig. 4d) indicated that u-Cu exhibits an upshift of the d-band center (−2.34 eV) relative to pristine Cu (−2.46 eV), leading to expedited interaction between the metal active center and the reaction intermediates. Consequently, as depicted in Fig. 4e, compared to pristine Cu, u-Cu transfers more electrons to the key intermediate of *NHO, resulting in stronger *NHO binding to reduce the $*NO \rightarrow *NHO$ energy barrier and boost the NO_2^--to-NH_3 energetics.[42]

As the HER is the major competitive reaction of NO_2RR,[43] the NO_2RR selectivity of u-Cu is studied by evaluating the competing adsorption between H and NO_2^- on u-Cu. As displayed in Fig. S11,† u-Cu adsorbs H (−0.41 eV) more weakly than NO_2^- (−1.15 eV), suggesting that NO_2^- can be more preferentially adsorbed on u-Cu to suppress the HER. Thus, the favorable NO_2^- adsorption and H repulsion make u-Cu highly selective towards the NO_2^--to-NH_3 conversion.

In conclusion, u-Cu is validated to be an effective NO_2RR catalyst with high durability, selectivity, and activity. Theoretical results uncover that the enhanced NO_2RR performance of u-Cu is attributed to the created undercoordinated Cu sites to promote NO_2RR energetics and suppress the HER. The present results demonstrate the exciting opportunity in the construction of undercoordinated metal sites to develop efficient NO_2RR catalysts for ammonia electrosynthesis.

Conflicts of interest

There are no conflicts of interest to declare.

Acknowledgements

This work is supported by the Natural Science Foundation of Gansu Province (23JRRA885).

References

1 W. Song, L. Yue, X. Fan, Y. Luo, B. Ying, S. Sun, D. Zheng, Q. Liu, M. S. Hamdy and X. Sun, *Inorg. Chem. Front.*, 2023, **10**, 3489–3514.
2 X. Zhao, G. Hu, G. F. Chen, H. Zhang, S. Zhang and H. Wang, *Adv. Mater.*, 2021, **33**, 2007650.
3 G. Qing, R. Ghazfar, S. T. Jackowski, F. Habibzadeh, M. M. Ashtiani, C.-P. Chen, M. R. Smith and T. W. Hamann, *Chem. Rev.*, 2020, **120**, 5437–5516.
4 Y. Li, H. Wang, C. Priest, S. Li, P. Xu and G. Wu, *Adv. Mater.*, 2021, **33**, 2000381.
5 H.-j. Chen, Z.-q. Xu, S. Sun, Y. Luo, Q. Liu, M. S. Hamdy, Z.-s. Feng, X. Sun and Y. Wang, *Inorg. Chem. Front.*, 2022, **9**, 4608–4613.
6 H. Chen, J. Liang, K. Dong, L. Yue, T. Li, Y. Luo, Z. Feng, N. Li, M. S. Hamdy, A. A. Alshehri, Y. Wang, X. Sun and Q. Liu, *Inorg. Chem. Front.*, 2022, **9**, 1514–1519.
7 Q. Liu, T. Xu, Y. Luo, Q. Kong, T. Li, S. Lu, A. A. Alshehri, K. A. Alzahrani and X. Sun, *Curr. Opin. Electrochem.*, 2021, **29**, 100766.
8 H. Chen, J. Liang, L. Li, B. Zheng, Z. Feng, Z. Xu, Y. Luo, Q. Liu, X. Shi, Y. Liu, S. Gao, A. M. Asiri, Y. Wang, Q. Kong and X. Sun, *ACS Appl. Mater. Interfaces*, 2021, **13**, 41715–41722.
9 K. Chu, X. Li, Q. Li, Y. Guo and H. Zhang, *Small*, 2021, **17**, 2102363.
10 K. Chen, G. Wang, Y. Guo, D. Ma and K. Chu, *Nano Res.*, 2023, **16**, 8737–8742.
11 J. Yuan, H. Yin, X. Jin, D. Zhao, Y. Liu, A. Du, X. Liu and A. P. O'Mullane, *Appl. Catal., B*, 2023, **325**, 122353.
12 W. Du, Z. Sun, K. Chen, F. Wang and K. Chu, *Chem. Eng. J.*, 2024, **481**, 148733.
13 Y. Wan, Y. Zhang, N. Zhang, Z. Zhang and K. Chu, *Chem. Eng. J.*, 2024, **481**, 148734.
14 J. Xiang, H. Zhao, K. Chen, X. Li, X. Li and K. Chu, *J. Colloid Interface Sci.*, 2024, **653**, 390–395.
15 J. Xiang, H. Zhao, K. Chen, X. Yang and K. Chu, *J. Colloid Interface Sci.*, 2024, **659**, 432–438.
16 X. Zhu, X. Fan, H. Lin, S. Li, Q. Zhai, Y. Jiang and Y. Chen, *Adv. Energy Mater.*, 2023, **13**, 2300669.
17 Y. Zhang, Y. Wang, L. Han, S. Wang, T. Cui, Y. Yan, M. Xu, H. Duan, Y. Kuang and X. Sun, *Angew. Chem., Int. Ed.*, 2023, **62**, e202213711.
18 S. Liu, L. Cui, S. Yin, H. Ren, Z. Wang, Y. Xu, X. Li, L. Wang and H. Wang, *Appl. Catal., B*, 2022, **319**, 121876.
19 G. Wang, Q. Chen, J. Zhang, X. An, Q. Liu, L. Xie, W. Yao, X. Sun and Q. Kong, *J. Colloid Interface Sci.*, 2023, **647**, 73–80.
20 Z. Ren, Q. Chen, J. Zhang, X. An, Q. Liu, L. Xie, W. Yao, X. Sun and Q. Kong, *Mater. Today Phys.*, 2023, **36**, 101162.
21 H. Qiu, Q. Chen, J. Zhang, X. An, Q. Liu, L. Xie, W. Yao, X. Sun and Q. Kong, *Inorg. Chem. Front.*, 2023, **10**, 3909–3915.
22 H. Wang, F. Zhang, M. Jin, D. Zhao, X. Fan, Z. Li, Y. Luo, D. Zheng, T. Li, Y. Wang, B. Ying, S. Sun, Q. Liu, X. Liu and X. Sun, *Mater. Today Phys.*, 2023, **30**, 100944.
23 L. Ouyang, X. Fan, Z. Li, X. He, S. Sun, Z. Cai, Y. Luo, D. Zheng, B. Ying and J. Zhang, *Chem. Commun.*, 2023, **59**, 1625–1628.
24 J. Liang, Z. Li, L. Zhang, X. He, Y. Luo, D. Zheng, Y. Wang, T. Li, H. Yan, B. Ying, S. Sun, Q. Liu, M. S. Hamdy, B. Tang and X. Sun, *Chem*, 2023, **9**, 1768–1827.
25 X. He, Z. Li, J. Yao, K. Dong, X. Li, L. Hu, S. Sun, Z. Cai, D. Zheng, Y. Luo, B. Ying, M. S. Hamdy, L. Xie, Q. Liu and X. Sun, *iScience*, 2023, **26**, 107100.

26 X. He, L. Hu, L. Xie, Z. Li, J. Chen, X. Li, J. Li, L. Zhang, X. Fang, D. Zheng, S. Sun, J. Zhang, A. Ali Alshehri, Y. Luo, Q. Liu, Y. Wang and X. Sun, *J. Colloid Interface Sci.*, 2023, **634**, 86–92.
27 X. Fan, D. Zhao, Z. Deng, L. Zhang, J. Li, Z. Li, S. Sun, Y. Luo, D. Zheng, Y. Wang, B. Ying, J. Zhang, A. A. Alshehri, Y. Lin, C. Tang, X. Sun and Y. Zheng, *Small*, 2023, **19**, 2208036.
28 X. Fan, X. He, X. Ji, L. Zhang, J. Li, L. Hu, X. Li, S. Sun, D. Zheng, Y. Luo, Y. Wang, L. Xie, Q. Liu, B. Ying and X. Sun, *Inorg. Chem. Front.*, 2023, **10**, 1431–1435.
29 X. Xu, L. Hu, Z. Li, L. Xie, S. Sun, L. Zhang, J. Li, Y. Luo, X. Yan, M. S. Hamdy, Q. Kong, X. Sun and Q. Liu, *Sustainable Energy Fuels*, 2022, **6**, 4130–4136.
30 X. Zhang, Y. Wang, Y. Wang, Y. Guo, X. Xie, Y. Yu and B. Zhang, *Chem. Commun.*, 2022, **58**, 2777–2787.
31 Q. Chen, X. An, Q. Liu, X. Wu, L. Xie, J. Zhang, W. Yao, M. S. Hamdy, Q. Kong and X. Sun, *Chem. Commun.*, 2022, **58**, 517–520.
32 L. Ouyang, L. Yue, Q. Liu, Q. Liu, Z. Li, S. Sun, Y. Luo, A. Ali Alshehri, M. S. Hamdy, Q. Kong and X. Sun, *J. Colloid Interface Sci.*, 2022, **624**, 394–399.
33 Z. Cai, D. Zhao, X. Fan, L. Zhang, J. Liang, Z. Li, J. Li, Y. Luo, D. Zheng and Y. Wang, *Small*, 2023, **19**, 2300620.
34 J. Liang, Q. Liu, A. A. Alshehri and X. Sun, *Nano Res. Energy*, 2022, **1**, e9120010.
35 H. Xu, Y. Ma, J. Chen, W.-x. Zhang and J. Yang, *Chem. Soc. Rev.*, 2022, **51**, 2710–2758.
36 Y. Wang, H. Li, W. Zhou, X. Zhang, B. Zhang and Y. Yu, *Angew. Chem., Int. Ed.*, 2022, **134**, e202202604.
37 K. Chen, J. Xiang, Y. Guo, X. Liu, X. Li and K. Chu, *Nano Lett.*, 2024, **24**, 541–548.
38 Y. Li, C. Cheng, S. Han, Y. Huang, X. Du, B. Zhang and Y. Yu, *ACS Energy Lett.*, 2022, **7**, 1187–1194.
39 H. Zhao, J. Xiang, G. Zhang, K. Chen and K. Chu, *Inorg. Chem. Front.*, 2023, **10**, 5950–5957.
40 W. Du, Y. Zhang, K. Chen, G. Zhang and K. Chu, *J. Cleaner Prod.*, 2023, **424**, 138875.
41 Y. Wan, W. Du, K. Chen, N. Zhang and K. Chu, *J. Colloid Interface Sci.*, 2023, **652**, 2180–2185.
42 F. Wang, H. Zhao, G. Zhang, H. Zhang, X. Han and K. Chu, *Adv. Funct. Mater.*, 2023, **34**, 2308072.
43 Y. Zhang, Y. Wan, X. Liu, K. Chen and K. Chu, *iScience*, 2023, **26**, 107944.